remote sensing

MDPI

Article

An Efficient Ground Moving Target Imaging Method for Synthetic Aperture Radar Based on Scaled Fourier Transform and Scaled Inverse Fourier Transform

Xin Zhang [1,2], Haoyu Zhu [1,2], Ruixin Liu [1,2], Jun Wan [1,2,*] and Zhanye Chen [3,4]

[1] School of Microelectronics and Communication Engineering, Chongqing University, Chongqing 400044, China
[2] Chongqing Key Laboratory of Space Information Network and Intelligent Information Fusion, Chongqing University, Chongqing 400044, China
[3] State Key Laboratory of Millimeter Waves, Southeast University, Nanjing 210096, China
[4] Institute of Electromagnetic Space, Southeast University, Nanjing 210096, China
* Correspondence: wanjun@cqu.edu.cn; Tel.: +86-023-65105925

Abstract: The unknown relative motions between synthetic aperture radar (SAR) and a ground moving target will lead to serious range cell migration (RCM) and Doppler frequency spread (DFS). The energy of the moving target will defocus, given the effect of the RCM and DFS. The moving target will easily produce Doppler ambiguity, due to the low pulse repetition frequency of radar, and the Doppler ambiguity complicates the corrections of the RCM and DFS. In order to address these issues, an efficient ground moving target focusing method for SAR based on scaled Fourier transform and scaled inverse Fourier transform is presented. Firstly, the operations based on the scaled Fourier transform and scaled inverse Fourier transforms are presented to focus the moving targets in consideration of Doppler ambiguity. Subsequently, in accordance with the detailed analysis of multiple target focusing, the spurious peak related to the cross term is removed. The proposed method can accurately eliminate the DFS and RCM, and the well-focused result of the moving target can be achieved under the complex Doppler ambiguity. Then, the blind speed sidelobe can be further avoided. The presented method has high computational efficiency without the step of parameter search. The simulated and measured SAR data are provided to demonstrate the effectiveness of the developed method.

Keywords: Doppler ambiguity; computationally efficient; scaled Fourier transform (SCFT); scaled inverse Fourier transform (SCIFT); synthetic aperture radar (SAR)

Citation: Zhang, X.; Zhu, H.; Liu, R.; Wan, J.; Chen, Z. An Efficient Ground Moving Target Imaging Method for Synthetic Aperture Radar Based on Scaled Fourier Transform and Scaled Inverse Fourier Transform. *Remote Sens.* **2024**, *16*, 2039. https://doi.org/10.3390/rs16112039

Academic Editors: Shuwen Xu, Luca Pallotta and Xiaolong Chen

Received: 6 May 2024
Revised: 1 June 2024
Accepted: 3 June 2024
Published: 6 June 2024

1. Introduction

Synthetic aperture radar (SAR) can image scenes of interest with high resolution without being affected by time and weather. SAR can be used in military reconnaissance, traffic monitoring, and other fields [1–10]. In the observed scene of interest, non-cooperative moving targets often appear. Therefore, in order to obtain the characteristics and information of the moving targets, the indication processing of the ground moving targets using synthetic aperture radar has become a research hotspot [11–18].

However, the unknown relative motion between the SAR platform and the moving target can cause range cell migration (RCM) and Doppler frequency spread (DFS), making it difficult to focus on the moving target [19,20]. RCM includes quadratic RCM (QRCM) and linear RCM (LRCM), caused by target along- and cross-track velocities, respectively. DFS induced by the along-track velocity will cause the target energy to be defocused along the azimuth Doppler frequency. Therefore, RCM and DFS should be effectively eliminated in order to obtain a well-focused result for the moving target [17–21]. In addition, due to the low pulse repetition frequency (PRF) of SAR, Doppler ambiguity easily exists in the moving target signal. Doppler ambiguity includes Doppler center blur and spectrum

ambiguity [20,22]. In the azimuth dimension, when the Doppler center shift (DCS) of the target signal is more than half that of the pulse repetition frequency, the target signal will produce Doppler center blur. On the other hand, when the Doppler spectrum of the target occupies two or more PRF bands, the target signal will produce Doppler spectrum splitting, resulting in Doppler spectrum blurring. Complex Doppler ambiguity (including Doppler spectrum and center ambiguity) complicates the correction of DFS and RCM.

The keystone transform (KT) [23–25] and the second-order keystone transform (SOKT) [26,27] are widely used in moving target focusing, which can compensate the LRCM or QRCM of a moving target without knowing the prior motion parameters of the moving target. Subsequently, the Doppler KT (DKT) is proposed [28], which can remove LRCM and QRCM. However, these methods (i.e., DKT, SKT, and KT) are troubled by DFS and Doppler ambiguity. In order to solve the problem of Doppler ambiguity and DFS, the 2D frequency matched filtering (2-DFMF) method based on the stationary phase principle has been proposed [21]. However, when the time–bandwidth product is small, the focusing performance of this method deteriorates dramatically. In order to solve the problem of the influence of DFS, a method combining KT and Doppler filter has been proposed [29]. Although this method can solve RCM and DFS at the same time, it requires a multi-dimensional parameter search and has great computational complexity. In addition, a method based on KT without parameter estimation has been proposed. Nevertheless, this method is affected by Doppler spectrum splitting [30]. In [31], considering the blurring of the Doppler spectrum, a piecewise KT-Doppler Lv's transform algorithm has been proposed. However, this algorithm verifies that the Doppler center shift operation used to solve the Doppler spectrum ambiguity will be invalid when the spectrum bandwidth is more than half that of PRF. In [20], a Deramp-KT processing (DKP) method based on instantaneous range-Doppler processing has been proposed. However, this method does not take into account the influence of the unknown along-track velocity of the moving target, which leads to serious coherent accumulation loss.

In addition, various multi-dimensional searching methods have been developed to obtain well-focused results, for example, radon-linear canonical transform [32], radon-fractional Fourier transform [33], and extended generalized radon Fourier transform [34]. However, considering the multi-dimensional parameter search operation, the computational complexity of these algorithms is very large. In order to reduce the amount of computational complexity, several one-dimensional search algorithms have been proposed, for example, modified SOKT (MSOKT) [17] and improved axis-rotation–time-reversal transform (IAR–TRT) [14]. Nevertheless, because the search operation is one-dimensional, these methods' computational costs are still high. In addition, the IAR–TRT method is affected by the aliasing of the scaled frequency spectrum, and the MSOKT approach suffers from the problem of blind speed sidelobe (BSSL).

On the basis of the previous work, a computationally efficient SAR ground moving target imaging method is proposed in this paper. Firstly, a second-order phase estimation method based on scaled Fourier transform (SCFT) is proposed. Secondly, an operation based on improved slow-time reversal transform and scaled inverse Fourier transform (ISTRT–SCIFT) is proposed for first-order phase estimation. Finally, according to the estimated parameters, the focusing matched function is constructed to focus the moving target. Furthermore, the features of cross terms related to the multiple target case are analyzed in detail, and the spurious peak identification procedure is presented to eliminate the effect of cross term. The processed results of the simulated and measured data show that the proposed method and the spurious peak identification procedure are effective.

The main contributions of this study can be summarized as follows: (1) The proposed approach can estimate the coefficients of the first- and second-order terms within only two steps, and the operation steps are relatively simple. (2) The proposed method has robust to complex Doppler ambiguity and avoids the searching operation of the Doppler ambiguity number. (3) The proposed method can address the BSSL problem. (4) The developed approach has a low computational cost because the parameter-searching step is avoided.

(5) The spurious peak identification method that eliminates the influence of cross terms is proposed based on a detailed analysis of multiple target focusing.

The remainder of this article is organized as follows: Section 2 introduces the proposed method. Section 3 provides the experimental results. Section 4 presents the discussion associated with the proposed method. Section 5 presents a summary of this paper.

2. Methods

2.1. Signal Model and Signal Characteristics

Figure 1 shows the geometric relationship between the ground moving target and the platform in the SAR side-looking operation mode. During the coherent cumulative time T_a, the point target moves from point A to point B. The platform flies along the straight line at speed v. v_a and v_c are the along-track velocity and the cross-track velocity of the target, respectively. R_0 represents the shortest slant range between the ground moving target and the SAR platform. t_n indicates the azimuth slow-time variable.

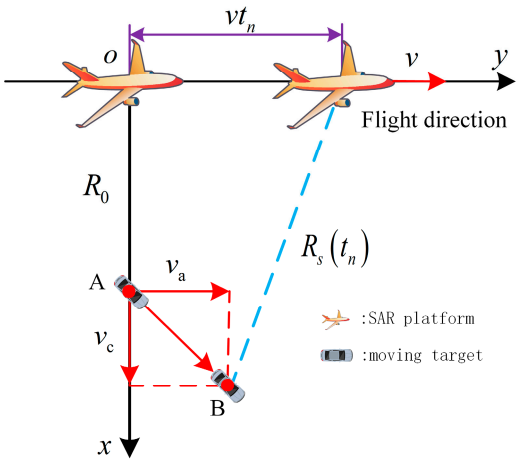

Figure 1. Motion geometric model between the moving target and the SAR platform.

Combined with the motion geometric model shown in Figure 1, on the basis of Taylor series expansion, the instantaneous slant range between the SAR and moving target can be expressed as follows:

$$\begin{aligned} R_s(t_n) &= \sqrt{(vt_n - v_a t_n)^2 + (R_0 - v_c t_n)^2} \\ &\approx R_0 - v_c t_n + \frac{(v-v_a)^2}{2R_0} {t_n}^2 \\ &= R_0 + \rho_0 t_n + \rho_1 {t_n}^2 \end{aligned} \tag{1}$$

where $\rho_0 = -v_c$ and $\rho_1 = (v - v_a)^2 / 2R_0$ represent the first and second coefficients of the distance's Taylor expansion, respectively.

The chirp signal emitted by the radar can be expressed as follows:

$$p(t) = rect(\frac{t}{T_p}) \exp(j\pi\gamma t^2) \exp(j2\pi f_c t) \tag{2}$$

where $rect(\frac{t}{T_p}) = \begin{cases} 1, |t| \le \frac{T_p}{2} \\ 0, |t| \ge \frac{T_p}{2} \end{cases}$ represents the rectangular window function; and T_P, f_c, t, and γ represent the pulse width, carrier frequency, range fast-time variable, and frequency modulation rate, respectively.

After range pulse compression processing [12,14,23], the model of the target echo signal in the range-frequency and azimuth slow-time domain can be expressed as follows:

$$s_1(f, t_n) = rect(\frac{f}{B}) \exp\left\{-\frac{j4\pi}{c}(f + f_c)\left[R_0 + \rho_0 t_n + \rho_1 t_n^2\right]\right\} \quad (3)$$

where c, f, and B are the speed of light, the range-frequency variable, and the bandwidth of the transmitted signal, respectively. In particular, the azimuth window function and signal amplitude are omitted for the convenience of algorithm derivation.

After the inverse Fourier transform (IFT) of the range dimension is applied to (3), the target echo signal in the range fast-time and azimuth slow-time can be obtained as follows:

$$s_1(t, t_n) = \sin c\left\{B\left[t - \frac{2R_0}{c} - \frac{2\rho_0 t_n}{c} - \frac{2\rho_1 t_n^2}{c}\right]\right\} \exp\left[-\frac{j4\pi}{\lambda}\left(R_0 + \rho_0 t_n + \rho_1 t_n^2\right)\right] \quad (4)$$

where $\sin c(x) = \sin(\pi x)/(\pi x)$ stands for the sinc function.

It can be seen from (4) that there is a serious coupling between the range time and azimuth time. In the sinc function term, the t_n-term and the t_n^2-term will cause the LRCM and the QRCM in the range dimension, respectively. RCM contains the LRCM and QRCM. In general, RCM will cause the target to be defocused along the range dimension. In addition, in the exponential term, the t_n-term will cause the DCS without causing the defocusing of the target energy, and the t_n^2-term will cause DFS, which will cause the defocusing of target energy along the azimuth Doppler frequency dimension. According to the analysis of the azimuth Doppler spectrum distribution characteristics, when the DCS exists for more than half of PRF, the signal will produce Doppler center blur, as exhibited in Figure 2a. As shown in Figure 2b,c, due to the existence of DCS and DFS, the target Doppler spectrum may occupy two or more PRF bands, resulting in Doppler spectrum splitting, that is, the phenomenon of Doppler spectrum ambiguity. f_{t_n}, f, and Δf_1 in the figure represent the azimuth Doppler frequency in respect to t_n, the range-frequency in respect to t, and the azimuth Doppler frequency offset caused by the azimuth time t_n, respectivley. The existence of Doppler ambiguity (including Doppler spectrum ambiguity and Doppler center blur) makes the compensation of RCM and DFS more difficult. Therefore, how to effectively compensate for RCM and DFS in the case of Doppler ambiguity is particularly critical.

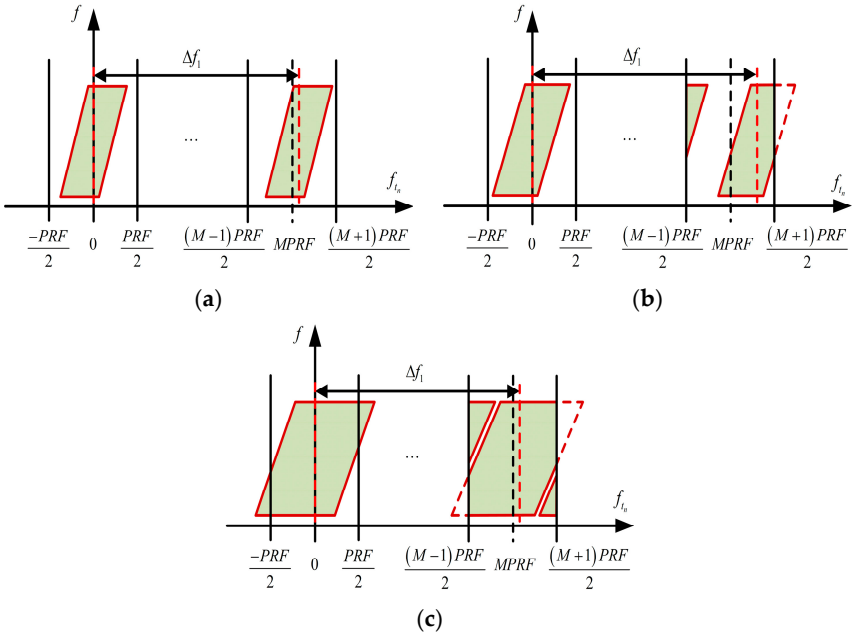

Figure 2. Azimuth Doppler spectrum distribution diagram. (**a**) The Doppler spectrum occupies a PRF band. (**b**) Doppler spectrum occupies two PRF bands. (**c**) Doppler spectrum occupies more PRF bands.

2.2. Description of the Proposed Algorithm

As shown in (3), the coupling of the first-order phase and the second-order phase makes the imaging of the moving target more complex. In order to eliminate the coupling effect between the first- and second-order phases, the slow-time reversal transform in the range-frequency is introduced, as follows:

$$\begin{aligned} s_2(f,t_n) &= s_1(f,t_n)s_1(f,\overleftarrow{t}_n) \\ &= s_1(f,t_n)s_1(f,-t_n) \\ &= rect(\tfrac{f}{B})\exp\left\{-\tfrac{j8\pi}{c}(f+f_c)\left[R_0+\rho_1 t_n^2\right]\right\} \end{aligned} \tag{5}$$

where "$\leftarrow$" represents the azimuth slow-time reversal transform.

As shown in (5), after slow-time reversal transform is performed, only the effects of the second-order phase (QRCM and DFS) remain, and the effects of the first-order phase (i.e., LRCM and DCS) can be eliminated. Therefore, in order to eliminate the QRCM and DFS simultaneously, the SCFT along the azimuth time domain is introduced, as follows:

$$\begin{aligned} s_2(f,f_\psi) &= \int s_2(f,t_n)\exp\left[-j2\pi f_\psi \varphi\left(\frac{f+f_c}{f_c}\right)t_n^2\right]dt_n^2 \\ &= rect\left(\frac{f}{B}\right)\exp\left[-\frac{j8\pi}{c}(f+f_c)R_0\right]\delta\left(f_\psi+\frac{4\rho_1}{\varphi\lambda}\right) \end{aligned} \tag{6}$$

After IFT is performed for (6) along the range-frequency dimension, we obtain the following:

$$s_2(t,f_\psi) = \mathrm{sinc}\left[B\left(t-\frac{4R_0}{c}\right)\right]\delta\left(f_\psi+\frac{4\rho_1}{\varphi\lambda}\right) \tag{7}$$

where φ, f_ψ, and $\delta(\cdot)$ indicate the scale zoom factor of SCFT, the scaled frequency variable after applying SCFT, and the Dirac function, respectively. The constant term is omitted in (7), given that it does not affect the result of the subsequent analysis. Unless otherwise specified, similar constant terms in the following equations are also omitted. The selection criteria of the scale zoom factor of SCFT are provided in [17]. The selection criteria for the scaling factor are detailed in Appendix A.

On the basis of peak position in (7), the second-order phase coefficient estimated value of the moving target is:$\hat{\rho}_1 = -\varphi\lambda\hat{f}_\psi/4$.

The second-order phase compensation function in the range-frequency and azimuth slow-time can be constructed by using the estimated second-order phase coefficient value, as follows:

$$H(f,t_n,\hat{\rho}_1) = \exp\left[\frac{j4\pi}{c}(f+f_c)\hat{\rho}_1 t_n^2\right] \tag{8}$$

After (8) is multiplied by (3), we obtain the following:

$$\begin{aligned} s_3(f,t_n) &= s_1(f,t_n)H(f,t_n,\hat{\rho}_1) \\ &= \mathrm{rect}\left(\tfrac{f}{B}\right)\exp\left[-\tfrac{\mathrm{j}4\pi}{c}(f+f_c)(R_0+\rho_0 t_n)\right] \end{aligned} \tag{9}$$

As shown in (9), the influence of the second-order phase of the target signal is effectively removed. Nevertheless, the first-order phase remains, and the LRCM caused by the first-order phase still exists. KT is usually performed in the traditional approaches. However, KT easily suffers from the problem of Doppler ambiguity. Therefore, in order to effectively remove LRCM in the presence of Doppler ambiguity, an operation based on ISTRT–SCIFT is proposed.

First, as shown in (9), the first-order phase ($\rho_0 t_n$-term) is coupled with the zero-order phase (i.e., R_0-term). To eliminate the zero-order phase and keep only the first-order phase, the ISTRT is proposed, as follows:

$$s_4(f,t_n) = s_3(f,t_n)s_3^*(f,\overleftarrow{t}_n) = \mathrm{rect}\left(\frac{f}{B}\right)\exp\left[-\frac{\mathrm{j}8\pi}{c}(f+f_c)\rho_0 t_n\right] \tag{10}$$

where $*$ stands for conjugate operation.

According to (10), although the coupling between the zero- and first-order phases is removed, there is still coupling between the azimuth slow-time and the range-frequency. Therefore, the SCIFT along the range-frequency variable is introduced, as follows:

$$\begin{aligned} s_4(t_\alpha,t_n) &= \int s_4(f,t_n)\exp(j4\pi t_\alpha t_n f)d(t_n f) \\ &= \delta\left(t_\alpha + \frac{2\rho_0}{c}\right)\exp\left(-\frac{\mathrm{j}8\pi}{\lambda}\rho_0 t_n\right) \end{aligned} \tag{11}$$

After FT is performed to (11) along the azimuth slow-time variable, we have the following:

$$s_4(t_\alpha, f_{t_n}) = \delta\left(t_\alpha + \frac{2\rho_0}{c}\right)\delta\left(f_{t_n} - \frac{4\rho_0}{\lambda}\right) \tag{12}$$

where t_α and f_{t_n} denote the scaled range time variable after performing SCIFT and the azimuth Doppler frequency variable, respectively.

In accordance with the peak position in (12), the estimated value of the first-order phase coefficient can be obtained as: $\hat{\rho}_0 = -\hat{t}_\alpha c/2$. Therefore, the effect of the BSSL is avoided for the proposed method, given that the searching operation of the first-order phase coefficient (i.e., radial velocity) is absent.

Then, with the estimated first- and second-order phase coefficients, the focus matching filter function can be constructed as follows:

$$H_1(f,t_n,\hat{\rho}_0,\hat{\rho}_1) = \exp\left(\frac{j4\pi f\hat{\rho}_0 t_n}{c}\right)\exp\left[\frac{j4\pi}{c}(f+f_c)\hat{\rho}_1 t_n^2\right] \tag{13}$$

Finally, after (13) is multiplied by (3), we can obtain the following:

$$\begin{aligned} s_5(f,t_n) &= s_1(f,t_n)H_1(f,t_n,\hat{\rho}_0,\hat{\rho}_1) \\ &= rect\left(\tfrac{f}{B}\right)\exp\left[-\tfrac{j4\pi}{c}(f+f_c)R_0\right]\exp\left(-\tfrac{j4\pi}{\lambda}\rho_0 t_n\right) \end{aligned} \tag{14}$$

After range IFT and azimuth FT are applied to (14), the final focused result of the target is as follows:

$$s_5(t,f_{t_n}) = \sin c\left[B\left(t - \frac{2R_0}{c}\right)\right]\sin c\left[T_i\left(f_{t_n} + \frac{2\rho_0}{\lambda}\right)\right] \tag{15}$$

where T_i represents the azimuth accumulation time.

A flow chart of the proposed method is provided in Figure 3.

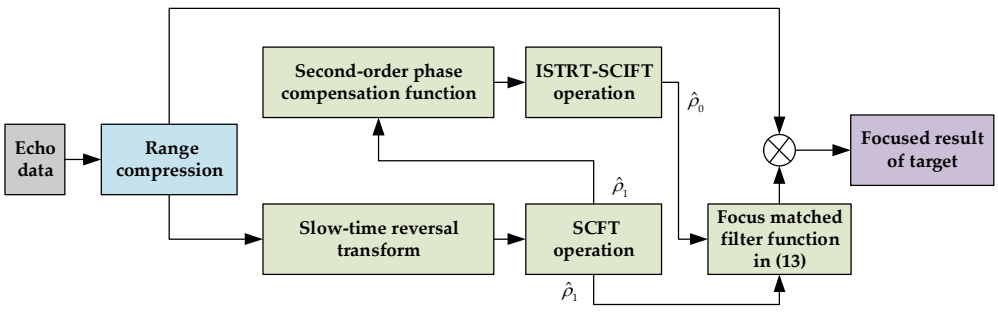

Figure 3. Flow chart of the proposed method.

2.3. Multiple Target Analysis

The above content analyzes the focusing situation of a single moving target, and it can be seen that this method can effectively focus the target. However, for the observation scene, multiple moving targets should be considered in the actual scenario. Therefore, the influence of cross terms related to multiple targets needs to be further studied. For the case of multiple targets, the signal in (3) can be expressed as follows:

$$s_{1,m}(f,t_n)=\sum_{i=1}^{G} rect(\frac{f}{B})\exp\left[-\frac{j4\pi}{c}(f+f_c)(R_{0,i}+\rho_{0,i}t_n+\rho_{1,i}t_n^2)\right] \tag{16}$$

where G indicates the number of moving targets and $R_{0,i}$ denotes the nearest slant range of the ith moving target. $\rho_{0,i}=-v_{c,i}$ and $\rho_{1,i}=(v-v_{a,i})/(2R_{0,i})$ denote the first- and second-order range model coefficients of the ith moving target, respectively.

After performing the operations in (5) to (16), we can obtain the following:

$$\begin{aligned} s_{2,m}(f,t_n) &= \underbrace{\sum_{i=1}^{G} rect(\frac{f}{B})\exp\left[-\frac{j8\pi}{c}(f+f_c)(R_{0,i}+\rho_{1,i}t_n^2)\right]}_{auto\ \text{terms}} \\ &+\sum_{i=1}^{G}\sum_{j=1j\neq i}^{G} rect(\frac{f}{B})\exp\left[-\frac{j4\pi}{c}(f+f_c)(R_{0,i}+R_{0,j})\right] \\ &\underbrace{\times\exp\left\{-\frac{j4\pi}{c}(f+f_c)\left[(\rho_{0,i}-\rho_{0,j})t_n+(\rho_{1,i}+\rho_{1,j})t_n^2\right]\right\}}_{cross\ \text{terms}} \end{aligned} \tag{17}$$

It can be seen from (17) that DCS and LRCM are effectively eliminated for the auto terms, while the effects of QRCM and DFS still exist. However, for cross terms, the influence of the first- and the second-order terms exists. The following will analyze the two cases of $\rho_{0,i}\neq\rho_{0,j}$ and $\rho_{0,i}=\rho_{0,j}$.

In the first case, when $\rho_{0,i}\neq\rho_{0,j}$, the cross terms are defocused, and the effective peak cannot be formed. The formation of auto term peaks is unaffected by the cross terms. Therefore, only the peak formed by the auto terms is needed to estimate the second-order phase coefficient.

According to SCFT processing, the estimated second-order phase coefficient of the moving target can be expressed as follows:

$$\hat{\rho}_{1,i}=-\varphi\lambda\hat{f}_{\psi}/4 \tag{18}$$

Using the estimated second-order phase coefficient, the second-order phase compensation function in the range-frequency domain and azimuth slow-time domain can be constructed as follows:

$$H_{2,m}(f,t_n,\hat{\rho}_{1,i})=\exp\left[\frac{j4\pi}{c}(f+f_c)\hat{\rho}_{1,i}t_n^2\right] \tag{19}$$

As the single target analysis above is the same, the influence of the second-order phase of the moving target signal is effectively removed. Nevertheless, the first-order phase remains, and the LRCM caused by the first-order phase still exists.

After the operations in (9) and (10) are performed to (16), we have the following:

$$\begin{aligned} s_{4,m}(f,t_n) &= [s_{1,m}(f,t_n)H_{2,m}(f,t_n,\hat{\rho}_{1,i})]\cdot\left[s_{1,m}(f,\overleftarrow{t}_n)H_{2,m}(f,\overleftarrow{t}_n,\hat{\rho}_{1,i})\right]^* \\ &= \underbrace{\sum_{i=1}^{G} rect(\frac{f}{B})\exp\left[-\frac{j8\pi}{c}(f+f_c)\rho_{0,i}t_n\right]}_{auto\ \text{terms}} \\ &\quad \underbrace{\begin{aligned} &+\sum_{i=1}^{G}\sum_{j=1j\neq i}^{G} rect(\frac{f}{B})\exp\left[-\frac{j4\pi}{c}(f+f_c)(R_{0,i}-R_{0,j})\right] \\ &\times\exp\left[-\frac{j4\pi}{c}(f+f_c)(\rho_{0,i}+\rho_{0,j})t_n\right] \\ &\times\exp\left[\frac{j4\pi}{c}(f+f_c)(\rho_{1,i}-\rho_{1,j})t_n^2\right] \end{aligned}}_{cross\ \text{terms}} \end{aligned} \tag{20}$$

According to (20), the DFS and QRCM of the auto terms are eliminated. The auto terms can be effectively focused and form obvious peaks after performing the SCIFT operation. In the cross term, when $R_{0,i} \neq R_{0,j}$ or $\rho_{1,i} \neq \rho_{1,j}$ are satisfied, the cross terms will be defocused after applying SCIFT operation. Therefore, as for this case, the determination of the auto terms' peak values is not influenced by the cross terms, and the target is focused after the matching function is constructed from the estimated parameters related to the self-term peak.

However, moving targets may have the same nearest slant range and azimuth velocity, i.e., $R_{0,j} = R_{0,i}$, $\rho_{1,i} = \rho_{1,j}$, in a particular situation. Then, the signal in (20) is rewritten as follows:

$$\begin{aligned} &s_{4,m}(f,t_n) \\ &= \underbrace{\sum_{i=1}^{G} rect(\frac{f}{B})\exp\left[-\frac{j8\pi}{c}(f+f_c)\rho_{0,i}t_n\right]}_{auto\ \text{terms}} \\ &\underbrace{+\sum_{i=1}^{G}\sum_{j=1j\neq i}^{G} rect(\frac{f}{B})\exp\left[-\frac{j4\pi}{c}(f+f_c)(\rho_{0,i}+\rho_{0,j})t_n\right]}_{cross\ \text{terms}} \end{aligned} \tag{21}$$

After SCIFT is performed to (21) along the range-frequency variable, we obtain the following:

$$\begin{aligned} s_{4,m}(t_\alpha,t_n) &= \int s_{4,m}(f,t_n)\exp(j4\pi t_\alpha t_n f)d(t_n f) \\ &= \underbrace{\sum_{i=1}^{G}\delta\left(t_\alpha+\frac{2\rho_{0,i}}{c}\right)\exp\left(-\frac{\mathrm{j}8\pi}{\lambda}\rho_{0,i}t_n\right)}_{auto\ \text{terms}} \\ &\quad \underbrace{+\sum_{i=1}^{G}\sum_{j=1j\neq i}^{G}\delta\left(t_\alpha+\frac{\rho_{0,i}+\rho_{0,j}}{c}\right)\exp\left(-\frac{\mathrm{j}4\pi}{\lambda}(\rho_{0,i}+\rho_{0,j})t_n\right)}_{cross\ \text{terms}} \end{aligned} \tag{22}$$

After FT is performed to (22) along the azimuth slow-time and the constant terms are omitted, we have the following:

$$\begin{aligned} s_{4,m}(t_\alpha, f_{t_n}) &= \underbrace{\sum_{i=1}^{G} \delta\left(t_\alpha + \frac{2\rho_{0,i}}{c}\right)\delta\left(f_{t_n} - \frac{4\rho_{0,i}}{\lambda}\right)}_{auto\ \text{terms}} \\ &\underbrace{+\sum_{i=1}^{G}\sum_{j=1 j\neq i}^{G} \delta\left(t_\alpha + \frac{\rho_{0,i}+\rho_{0,j}}{c}\right)\delta\left(f_{t_n} - \frac{2(\rho_{0,i}+\rho_{0,j})}{\lambda}\right)}_{cross\ \text{terms}} \end{aligned} \tag{23}$$

As shown in (23), the locations of the focused peak of the auto terms are $t_\alpha = -2\rho_{0,i}/c$ and $f_{t_n} = 4\rho_{0,i}/\lambda$, and the locations of the focused peak of the cross terms are $t_\alpha = -\rho_{0,i} + \rho_{0,j}/c$ and $f_{t_n} = 2(\rho_{0,i} + \rho_{0,j})/\lambda$. Therefore, the estimated first-order phase coefficient of the auto terms and cross terms are $\hat{\rho}_{0,i} = -\hat{t}_\alpha c/2$ and $\hat{\rho}_{0,i,j} = \rho_{0,i} + \rho_{0,j} = -\hat{t}_\alpha c$, respectively.

Then, based on the first- and second-order phase coefficients estimated by the auto terms and cross terms, the corresponding focusing matched functions are constructed as follows:

$$H_{3,auto}(f, t_n, \hat{\rho}_{0,i}, \hat{\rho}_{1,i}) = \exp\left(\frac{j4\pi f\hat{\rho}_{0,i}t_n}{c}\right)\exp\left[\frac{j4\pi}{c}(f+f_c)\hat{\rho}_{1,i}t_n^2\right] \tag{24}$$

$$H_{3,cross}(f, t_n, \hat{\rho}_{0,i,j}, \hat{\rho}_{1,i}) = \exp\left(\frac{j4\pi f\hat{\rho}_{0,i,j}t_n}{c}\right)\exp\left[\frac{j4\pi}{c}(f+f_c)\hat{\rho}_{1,i}t_n^2\right] \tag{25}$$

Compared with the expressions in (24) and (25), an extra defocusing term exists in (25), as follows:

$$\exp(\frac{j4\pi f\rho_{0,j}t_n}{c}) \tag{26}$$

Finally, after (16) is multiplied by (24) or (25) for auto terms or cross terms, respectivley, the corresponding results are written as follows:

$$\begin{aligned} s_{5,auto}(f, t_n) &= s_{1,m}(f, t_n)H_{3,auto}(f, t_n, \hat{\rho}_{0,i}, \hat{\rho}_{1,i}) \\ &= \sum_{i=1}^{G} rect\left(\frac{f}{B}\right)\exp\left[-\frac{j4\pi}{c}(f+f_c)R_{0,i}\right]\exp\left(-\frac{j4\pi}{\lambda}\rho_{0,i}t_n\right) \end{aligned} \tag{27}$$

$$\begin{aligned} s_{5,cross}(f, t_n) &= s_{1,m}(f, t_n)H_{3,cross}(f, t_n, \hat{\rho}_{0,i,j}, \hat{\rho}_{1,i}) \\ &= \sum_{i=1}^{G} rect\left(\frac{f}{B}\right)\exp\left[-\frac{j4\pi}{c}(f+f_c)R_{0,i}\right]\exp\left(-\frac{j4\pi f_c}{c}\rho_{0,i}t_n\right) \\ &\times \exp\left(\frac{j4\pi f}{c}\rho_{0,j}t_n\right) \end{aligned} \tag{28}$$

After range IFT and azimuth FT are applied to (27) and (28), the final moving target focusing result can be obtained as follows:

$$s_{5,auto}(t, f_{t_n}) = \sum_{i=1}^{G} \sin c\left[B(t - \frac{2R_{0,i}}{c})\right]\sin c\left[T_i(f_{t_n} + \frac{2\rho_{0,i}}{\lambda})\right] \tag{29}$$

$$s_{5,cross}(t, f_{t_n}) = \sum_{i=1}^{G}\sum_{j=1 j\neq i}^{G} \sin c\left[B(t - \frac{2R_{0,i}}{c} + \frac{2\rho_{0,j}t_n}{c})\right]\sin c\left[T_i(f_{t_n} + \frac{2\rho_{0,i}}{\lambda})\right] \tag{30}$$

Comparing (29) and (30), the signal in (30) indicates that the effect of LRCM still remains. Therefore, if the filter function is constructed using the cross term parameters, the obvious peaks are absent. However, the filter function constructed with the auto term

parameters can obtain obvious peaks, because there is no defocus term in (26). Therefore, in the above cases, the proposed algorithm can further eliminate the effect of the cross term.

In the second case, when $\rho_{0,i} = \rho_{0,j}$, the signal in (17) can be rewritten as follows:

$$\begin{aligned} s_{2,m}(f,t_n) &= \underbrace{\sum_{i=1}^{G} rect(\frac{f}{B}) \exp\left[-\frac{j8\pi}{c}(f+f_c)(R_{0,i}+\rho_{1,i}t_n^2)\right]}_{\text{auto terms}} \\ &+ \sum_{i=1}^{G}\sum_{j=1 j\neq i}^{G} rect(\frac{f}{B}) \exp\left[-\frac{j4\pi}{c}(f+f_c)(R_{0,i}+R_{0,j})\right] \\ &\underbrace{\times \exp\left\{-\frac{j4\pi}{c}(f+f_c)(\rho_{1,i}+\rho_{1,j})t_n^2\right\}}_{\text{cross terms}} \end{aligned} \tag{31}$$

After SCFT is performed to (31) along the azimuth-frequency variable, we obtain the following:

$$\begin{aligned} s_{2,m}(f,f_\psi) &= \int s_{2,m}(f,t_n) \exp\left[-j2\pi f_\psi \varphi\left(\frac{f+f_c}{f_c}\right)t_n^2\right] dt_n^2 \\ &= \underbrace{\sum_{i=1}^{G} rect\left(\frac{f}{B}\right) \exp\left[-\frac{j8\pi}{c}(f+f_c)R_{0,i}\right]\delta\left(f_\psi + \frac{4\rho_{1,i}}{\varphi\lambda}\right)}_{\text{auto terms}} \\ &+ \underbrace{\sum_{i=1}^{G}\sum_{j=1 j\neq i}^{G} \begin{matrix} rect\left(\frac{f}{B}\right) \exp\left[-\frac{j4\pi}{c}(f+f_c)(R_{0,i}+R_{0,j})\right] \\ \times\delta\left(f_\psi + \frac{2(\rho_{1,i}+\rho_{1,j})}{\varphi\lambda}\right) \end{matrix}}_{\text{cross terms}} \end{aligned} \tag{32}$$

After IFT is performed to (32) along the range-frequency variable, we obtain the following:

$$\begin{aligned} s_{2,m}(t,f_\psi) &= \underbrace{\sum_{i=1}^{G} \text{sinc}\left[B\left(t-\frac{4R_{0,i}}{c}\right)\right]\delta\left(f_\psi+\frac{4\rho_{1,i}}{\varphi\lambda}\right)}_{\text{auto terms}} \\ &+ \underbrace{\sum_{i=1}^{G}\sum_{j=1 j\neq i}^{G} \text{sinc}\left\{B\left[t-\frac{2(R_{0,i}+R_{0,j})}{c}\right]\right\}\delta\left[f_\psi+\frac{2(\rho_{1,i}+\rho_{1,j})}{\varphi\lambda}\right]}_{\text{cross terms}} \end{aligned} \tag{33}$$

As shown in (33), both the auto term and the cross term can form valid peaks. Therefore, the estimated second-order phase coefficients based on the auto term and the cross term are $\hat{\rho}_{1,i} = -\varphi\lambda f_\psi/4$ and $\hat{\rho}_{1,i,j} = \hat{\rho}_{1,i} + \hat{\rho}_{1,j} = -\varphi\lambda f_\psi/2$, respectively.

Then, based on the second-order phase coefficient estimated by the auto terms and cross terms, the corresponding focusing matched functions are constructed as follows:

$$H_{4,m,auto}(f,t_n,\hat{\rho}_{1,i}) = \exp\left[\frac{j4\pi}{c}(f+f_c)\hat{\rho}_{1,i}t_n^2\right] \tag{34}$$

$$H_{4,m,cross}(f,t_n,\hat{\rho}_{1,i,j}) = \exp\left[\frac{j4\pi}{c}(f+f_c)\hat{\rho}_{1,i,j}t_n^2\right] \tag{35}$$

After (16) is multiplied by (34) or (35) for the auto terms or cross terms, respectivley, the corresponding results are written as follows:

$$\begin{aligned} s_{3,m,auto}(f,t_n) &= s_{1,m}(f,t_n)H_{4,m,auto}(f,t_n,\hat{\rho}_{1,i}) \\ &= \underbrace{rect(\frac{f}{B})\exp\left[-\frac{j4\pi}{c}(f+f_c)(R_{0,i}+\rho_{0,i}t_n)\right]}_{auto\ \text{terms}} \\ &+ \underbrace{\sum_{j=1 j\neq i}^{G}\exp\left\{-\frac{j4\pi}{c}(f+f_c)\left[R_{0,j}+\rho_{0,j}t_n+(\rho_{1,i}-\rho_{1,j})t_n^2\right]\right\}}_{cross\ \text{terms}} \end{aligned} \tag{36}$$

$$\begin{aligned} s_{3,m,cross}(f,t_n) &= s_{1,m}(f,t_n)H_{4,m,cross}(f,t_n,\hat{\rho}_{1,i,j}) \\ &= \underbrace{rect(\frac{f}{B})\exp\left[-\frac{j4\pi}{c}(f+f_c)(R_{0,i}+\rho_{0,i}t_n-\hat{\rho}_{1,j}t_n^2)\right]}_{auto\ \text{terms}} \\ &+ \underbrace{\sum_{j=1 j\neq i}^{G}\exp\left\{-\frac{j4\pi}{c}(f+f_c)\left[R_{0,j}+\rho_{0,j}t_n+(\rho_{1,i}-\rho_{1,i,j})t_n^2\right]\right\}}_{\text{cross terms}} \end{aligned} \tag{37}$$

Comparing (36) and (37), it can be seen that, in the auto-term of (36), the influence of DFS and QRCM caused by the second-order phase has been eliminated. Similar to the analysis of the case of $\rho_{0,i} \neq \rho_{0,j}$, when $R_{0,i} \neq R_{0,j}$ or $\rho_{1,i} \neq \rho_{1,j}$ are satisfied, the first-order phase coefficient can be estimated by SCIFT. Similar to the analysis of the case of $\rho_{0,i} \neq \rho_{0,j}$, after the matched filtering function in (13) constructed by the estimation value related to the cross term is performed to (16), the influence of the second-order phase still exists, and the DFS and QRCM cannot be eliminated. Finally, the effective focusing result of the moving target cannot be obtained. Therefore, in this case, the proposed algorithm can still reject the effect of the cross term.

In summary, although the influence of the cross terms may be introduced in processing steps (5) and (10), only the focusing matching function in (13) constructed using the auto terms' estimation parameters can obtain the final focusing result. When the focus matching filter function is constructed using the parameters estimated by the cross terms, it cannot obtain the final focus result. According to the above phenomena, the wrong parameters estimated by the cross term can be identified, and the spurious peaks can be suppressed. In addition, the proposed operation for the identification of spurious peaks includes the nonlinear transform. If the intensity of the background is high (i.e., a low signal-to-noise ratio (SNR) circumstance), the performance of the nonlinear transform will significantly degrade. The presented operation of the spurious peak identification is not suitable for the low SNR circumstance.

In the following explanation, two simulation examples are presented to demonstrate the above analysis for multiple target focusing and spurious peak identification procedures. The parameters of simulated SAR are provided as follows:$f_c = 10$ GHz, $B = 200$ MHz, and $PRF = 1200$ Hz.

As for Case A, two target signals, indicated by TA and TB, with different first-order parameters are considered for simplicity. The simulated first- and second-order parameters of TA and TB are set as follows: $\rho_{0,TA} = -27.5$ m/s and $\rho_{1,TA} = 1.21$ m/s^2 for TA; $\rho_{0,TB} = -4.6$ m/s and $\rho_{1,TB} = 1.21$ m/s^2 for TB.

Figure 4 shows the results of Case A. Figure 4a shows the results of range compression for TA and TB. Two curved trajectories related to TA and TB are shown in the figure. The result after applying SCFT operation is shown in Figure 4b. Two peaks, with respect to TA and TB, are superposed together, as shown in Figure 4b. The results after the SCIFT and phase compensation operations are shown in Figure 4c. The figure shows three obvious peaks, denoted by TA, TB, and TC. Then, the recognition procedures for spurious peaks are adopted. The matching filter functions are constructed by using the peaks of TA, TB, and

TC shown in Figure 4c, respectively, to focus the moving targets. The well-focused results of TA and TB obtained by the method proposed in this paper are shown in Figure 4d,e. Figure 4f shows the results of defocus, which verify the previous judgment that TC is a spurious peak.

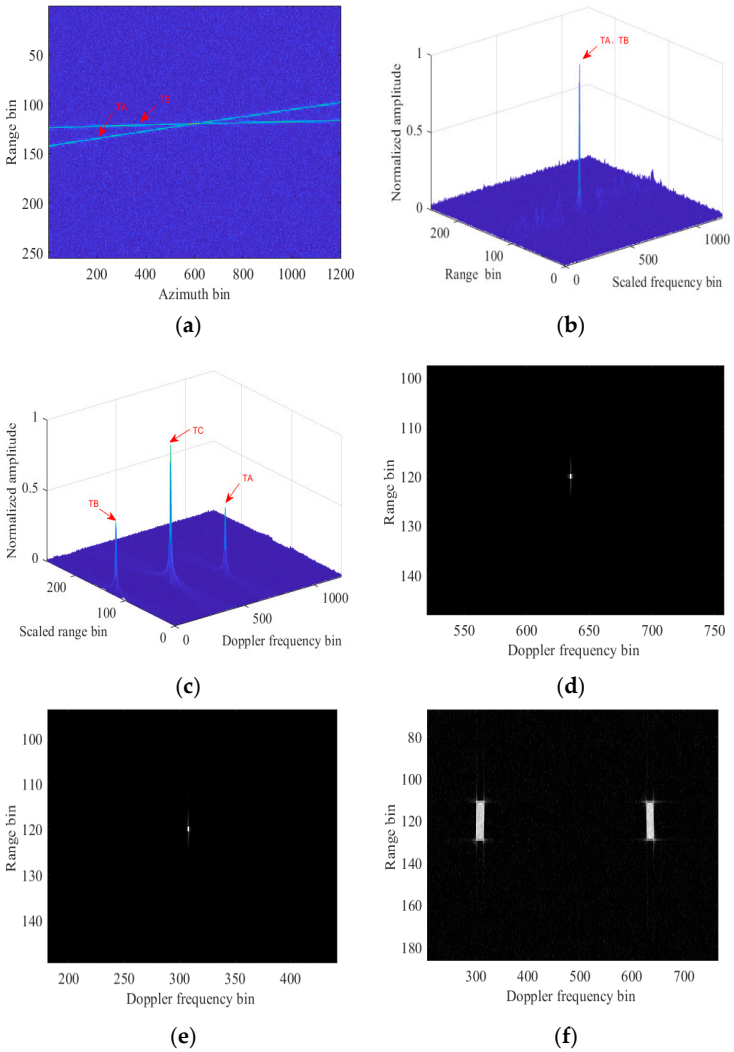

Figure 4. Experimental results of Case A. (**a**) Results after range compression for TA and TB. (**b**) Results after SCFT operation. (**c**) Results after SCIFT operation. (**d**) Focusing results using the auto term peak TA parameter. (**e**) Focusing results using the auto term peak TB parameter. (**f**) Focusing results using the cross term peak TC parameter.

As for Case B, two target signals—indicated by TD and TE—with different second-order parameters, are considered for simplicity. The simulated first- and second-order parameters of TD and TE are set as follows: $\rho_{0,TD} = -5.2$ m/s and $\rho_{1,TD} = 1.21$ m/s^2 for TD; $\rho_{1,TE} = -5.2$ m/s and $\rho_{1,TE} = 1.52$ m/s^2 for TE.

The experimental results of Case B are shown in Figure 5. Figure 5a shows the results after range compression for TD and TE. Figure 5b shows three evident peaks, represented by TD, TE, and TF, respectively. There are two auto term peaks and one cross term peak among the three peaks. The results after SCIFT and phase compensation operations are shown in Figure 5c. Two peaks with respect to TD and TE superposed together are shown in Figure 5c. The well-focused results of TD and TE obtained using the auto term parameters are shown in Figure 5d,e. Figure 5f shows the results of defocus, which verify the previous judgment that TF is a spurious peak.

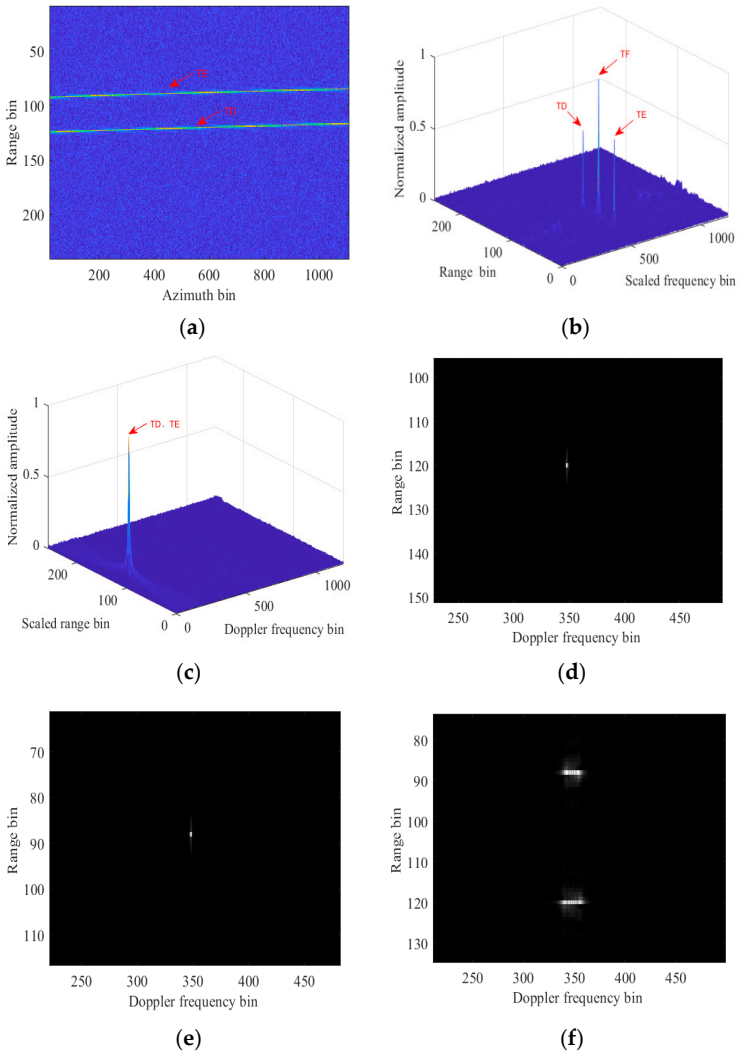

Figure 5. Experimental results of Case B. (**a**) Results after range compression for TD and TE. (**b**) Results after SCFT operation. (**c**) Results after SCIFT operation. (**d**) Focusing results using the auto term peak TD parameter. (**e**) Focusing results using the auto term peak TE parameter. (**f**) Focusing results using the cross term peak TF parameter.

3. Results

3.1. Simulated Results

Table 1 shows the main parameters of radar. Three moving targets are set in the experiment, which are Target A, Target B, and Target C, respectively. The simulated parameters of the three moving targets are shown in Table 2. According to the targets' simulated parameters, Targets A and C are the targets with Doppler center blur, and Target B is the target with Doppler spectrum ambiguity.

Table 1. Main radar parameters.

Parameters	Value
Carrier frequency	10 GHz
Range bandwidth	200 MHz
Pulse repetition frequency	1200 Hz
Radar platform velocity	140 m/s
Nearest slant range	5000 m
Azimuth accumulation time	1 s

The experimental results are shown in Figure 6. Figure 6a shows the three curve tracks of Targets A, B, and C after range pulse compression. It can be seen from the figure that the trajectory shows obvious RCM (including LRCM and QRCM). Figure 6b shows the Doppler spectra of the three moving targets. Due to the effect of DFS, the energy of the targets is distributed in several Doppler cells, resulting in the defocusing of targets' energy in the Doppler dimension. Furthermore, the Doppler spectrum of Targets A and C completely occupy a PRF band, while the Doppler spectrum of Target B occupies two adjacent PRF bands. These complex Doppler spectral distributions make it difficult to focus the moving target. The results after using the SCFT operation are shown in Figure 6c, forming three obvious peaks. Then, after phase compensation and SCIFT operation, the corresponding results are shown in Figure 6d, where three obvious peaks can be observed. The first- and second-order phase coefficients of the moving targets can be estimated from the peak values shown in Figure 6c,d. Thus, the matched filter function (24) of the moving target can be constructed. Finally, after matched filter function processing, the focusing results of Targets A, B, and C are obtained, as shown in Figure 6e,g,i, respectively. The results of focusing on Target B using the DKP method [20] are shown in Figure 6k,l. In this method, the influence of the along-track velocity of the moving targets is ignored, the target energy shows obvious defocusing, and the focusing performance is significantly reduced. Figure 6m shows the result of using the keystone (KT)-based method [30] to compensate for the LRCM of Target B. Since the target spectrum is distributed in two PRF bands, and the keystone is directly applied to LRCM compensation, the target trajectory after compensation is split into two parts. The compensation of target LRCM will be affected by trajectory splitting, resulting in serious coherent integration loss. It can be seen from the figure that this method is easily affected by the presence of Doppler spectrum splitting. Figure 6n shows the focusing results for Target B using the 2-DFMF method [21]. It can be seen from the results that the focusing effect of this method is affected when the azimuth velocity of the targets cannot be ignored. It can be seen from the above comparative experiments that, when there are Doppler ambiguity targets in the scene, defocused results are achieved for the KT-based method, the DKP method, and the method shown in [21]. However, a well-focused result can still be achieved for the method proposed in this paper. In order to compare it with the MSOKT method, the output SNRs of the proposed method and the MSOKT method are provided in Table 3. As shown in Table 3, the performance of the proposed method is similar to that of the MSOKT method under the relatively high SNR circumstance. However, in comparison with the MSOKT method, the proposed method can avoid the complex parameter-searching steps and has a low computational complexity. Moreover, the proposed method can also avoid the effect of BSSL. In addition, the performance of the proposed method significantly decreases under the low SNR condition, given that the nonlinear transform is used to reduce the computational complexity.

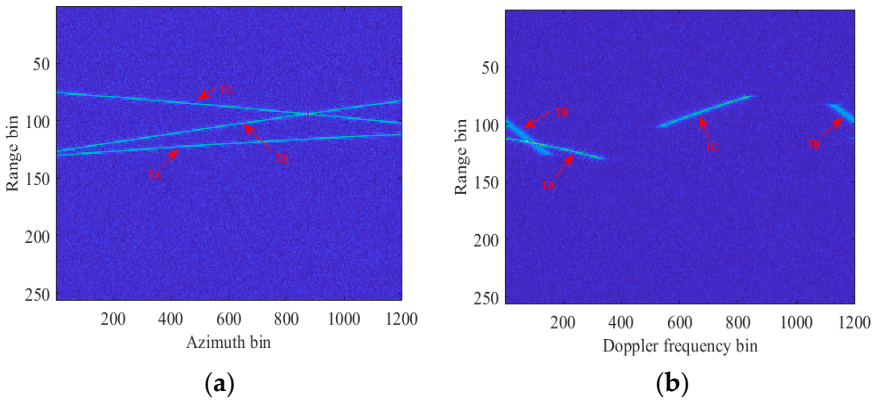

(**a**) (**b**)

Figure 6. *Cont.*

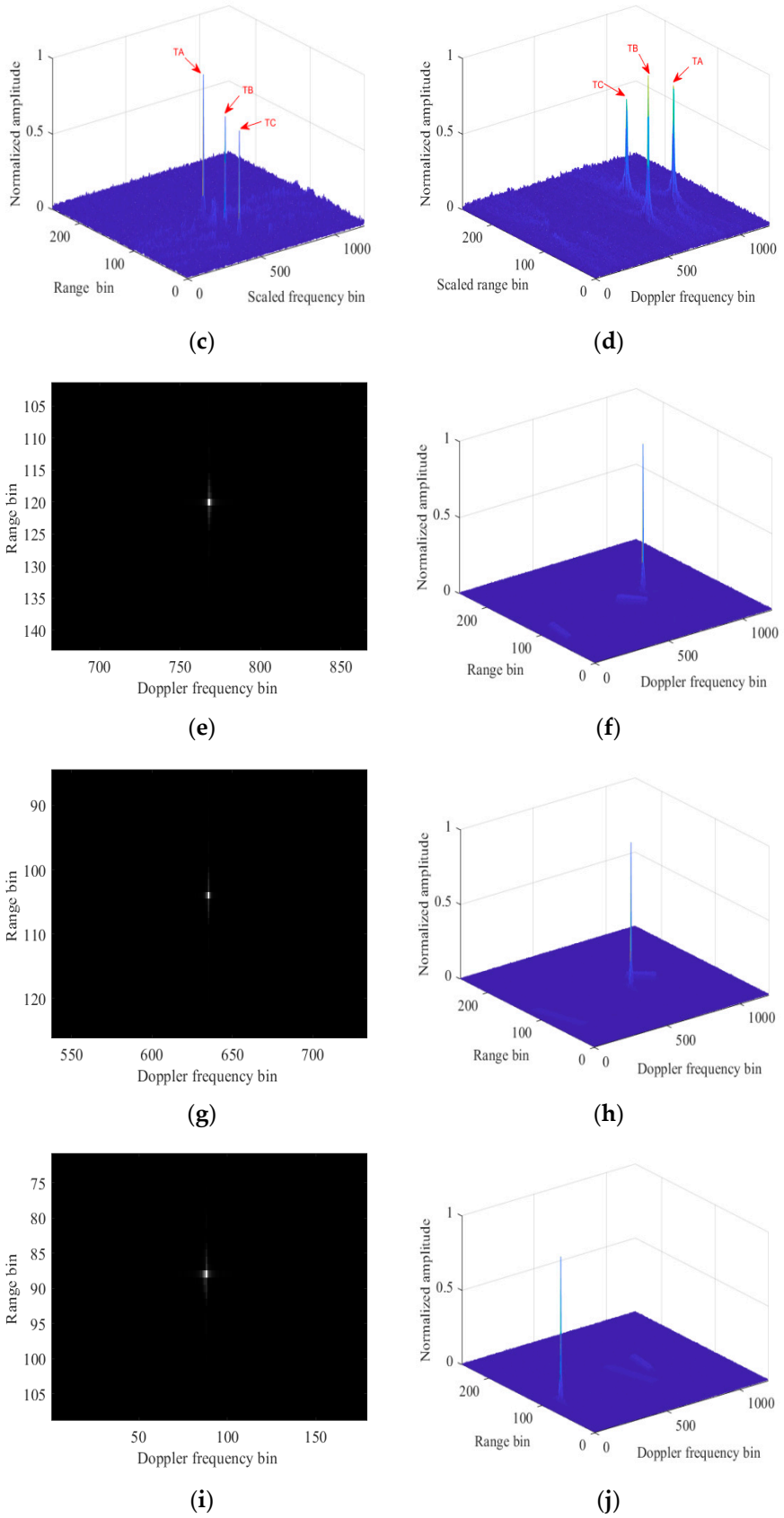

Figure 6. *Cont.*

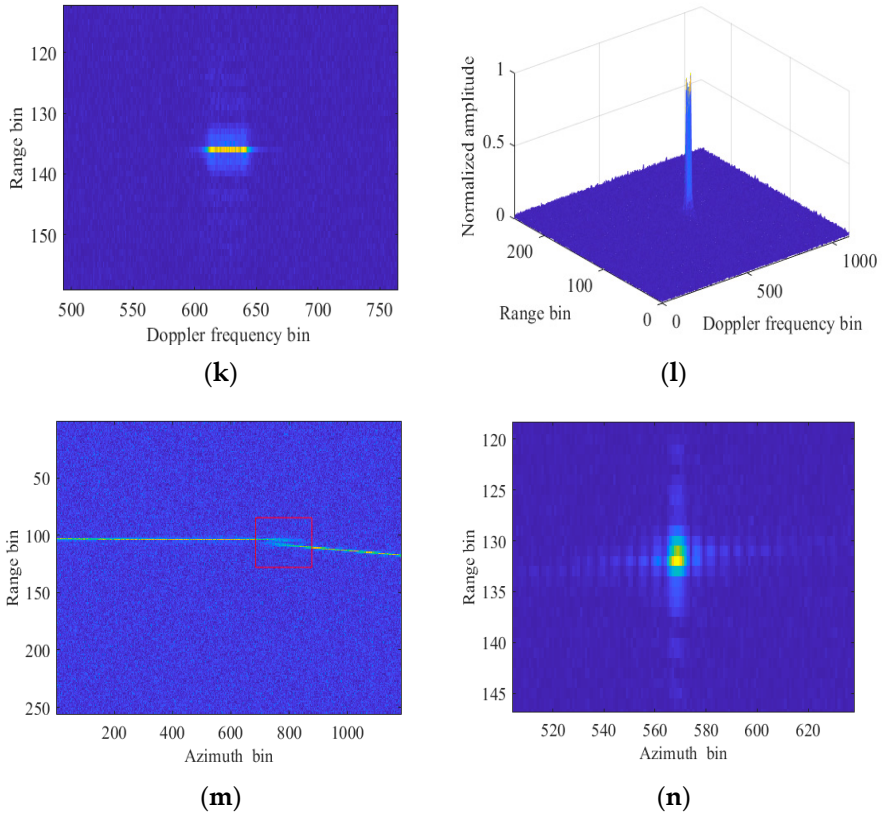

Figure 6. The results of the experiment. (**a**) Range compression results. (**b**) Doppler spectrum of three targets. (**c**) Results after SCFT operation. (**d**) Results of SCIFT. (**e**) Focusing result of TA using the proposed method. (**f**) Stereogram of Figure 6e. (**g**) Focusing result of TB by the developed method. (**h**) Stereogram of Figure 6g. (**i**) Focus result of TC by the developed method. (**j**) Stereogram of Figure 6i. (**k**) Results after TB is processed by the method in [20]. (**l**) Stereogram of Figure 6k. (**m**) Compensation result for LRCM using the keystone-based method for TB [30]. (**n**) Results after TB is processed by the method in [21].

Table 2. Target motion parameters of simulation.

	Along-Track Velocity (v_a)	**Cross-Track Velocity (v_c)**
Target A	−20.6 m/s	11.5 m/s
Target B	10 m/s	27.5 m/s
Target C	−12.5 m/s	−16.7 m/s

Table 3. Output SNRs of the proposed and MSOKT methods.

Input SNR (after Range Compression)	**Output SNR of Proposed Method**	**Output SNR of MSOKT Method**
13 dB	43.9724 dB	43.8633 dB
6 dB	37.0187 dB	36.9487 dB
0 dB	18.1273 dB	29.8408 dB

Overall, the experimental results show that the proposed algorithm can accurately compensate RCM and DFS induced by the unknown motion of the moving target in the presence of Doppler ambiguity and can obtain a well-focused result. The proposed algorithm is robust to complex azimuth Doppler ambiguity (including spectrum blur and Doppler center blur). Additionally, the developed method has a low computational burden because of its implementation steps without the parameter-searching operations (including the Doppler ambiguity number searching).

3.2. Spaceborne Real Data Results

In this sub-section, two segments of C-band spaceborne data collected by the RADARSAT-1 system are processed to verify the processing performance of the developed method. The basis radar parameters are provided in Table 4. In addition, the detailed parameters of SAR data are given in [1].

Table 4. Basis radar parameters of spaceborne real data.

Parameters	Value
Carrier frequency	5.3 GHz
Range bandwidth	30.116 MHz
Pulse repetition frequency	1236.98 Hz

(1) Single moving target processing results: Figure 7a shows the range pulse compression results of the selected target, which show that the target trajectory spans multiple range units, resulting in range migration, showing serious defocusing. Figure 7b shows the Doppler spectrum distribution of the moving target in the range time domain of the azimuth Doppler domain. It can be seen in the image that the energy is distributed in multiple azimuth Doppler units, which results in the severe defocusing of the moving target in the azimuth Doppler dimension. A significant peak appears after the SCFT-based operations, as shown in Figure 7c. Then, the result after the application of the SCIFT-based processing is shown in Figure 7d, and an obvious peak appears. According to the peak values shown in Figure 7c,d, the first- and second-order phase coefficients can be estimated, and then the matched filter function can be constructed according to the obtained parameters to focus the target. The corresponding focusing results are shown in Figure 7e,f. The result of processing using the method detailed in [17] is shown in Figure 7g. Compared with the algorithm shown in [17], the approach developed in this paper can avoid the influence of BSSL. As shown in Figure 7h, the processing result obtained using the method detailed in [14] has an obvious defocusing phenomenon along the azimuth dimension because of the effect of the scaled spectrum aliasing. Therefore, the method proposed in this paper has a better focusing performance than the methods in detailed [14,17]. Then, the estimated relative radial velocity (ρ_0) and acceleration ($2\rho_1$) of the target are provided, as follows: -204.0839 m/s and 50.2440 m/s^2. The results of the parameter estimation are consistent with the results found in [31]. Therefore, the above results of parameter estimation prove the effectiveness and accuracy of the proposed method.

(2) Two moving targets' processing results: The processing results of two moving targets are shown in Figure 8. Figure 8a shows two curved tracks of T1 and T2 after range compression, and obvious RCM (LRCM and QRCM) can be seen. The Doppler spectra of the two moving targets are shown in Figure 8b. It can be seen that, due to the effect of DFS, the target energy is distributed in multiple azimuth Doppler bins, which leads to the defocusing of the target energy in the Doppler dimension. Figure 8c shows the results of applying the SCFT operation. There are three distinct peaks in Figure 8c. After the operation based on the phase compensation function and SCIFT, the corresponding results are shown in Figure 8d, in which a target peak can be obtained. Through the peaks shown in Figure 8c,d, the first-order and second-order phase coefficients of the moving targets can be obtained, and the matched filtering function of the moving targets can be constructed. Then, as shown in Figure 8e, the focus results of T1 and T2 are obtained by using the constructed matched filter function. The processing results of the real spaceborne data above prove the performance of the method used for imaging multiple moving targets and the effectiveness of the spurious peak recognition operation proposed in this paper.

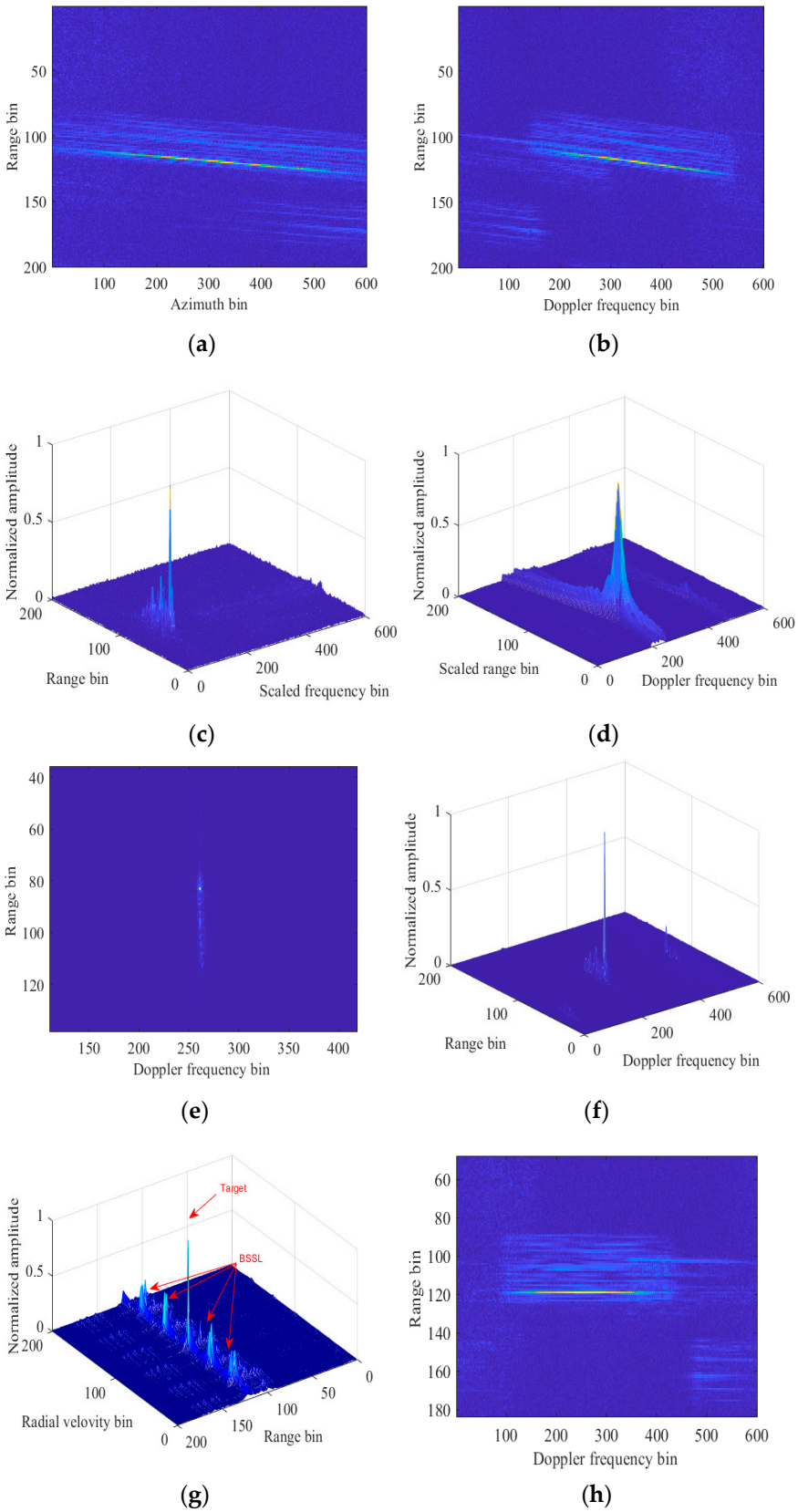

Figure 7. Results of spaceborne real data for a single target. (**a**) Results of range compression. (**b**) Doppler spectrum of moving target. (**c**) Result after SCFT operation. (**d**) Result after SCIFT operation. (**e**) Focusing result of the target by the developed approach. (**f**) Stereogram of Figure 7e. (**g**) Results of processing with the method in [17]. (**h**) Results of processing with the method in [14].

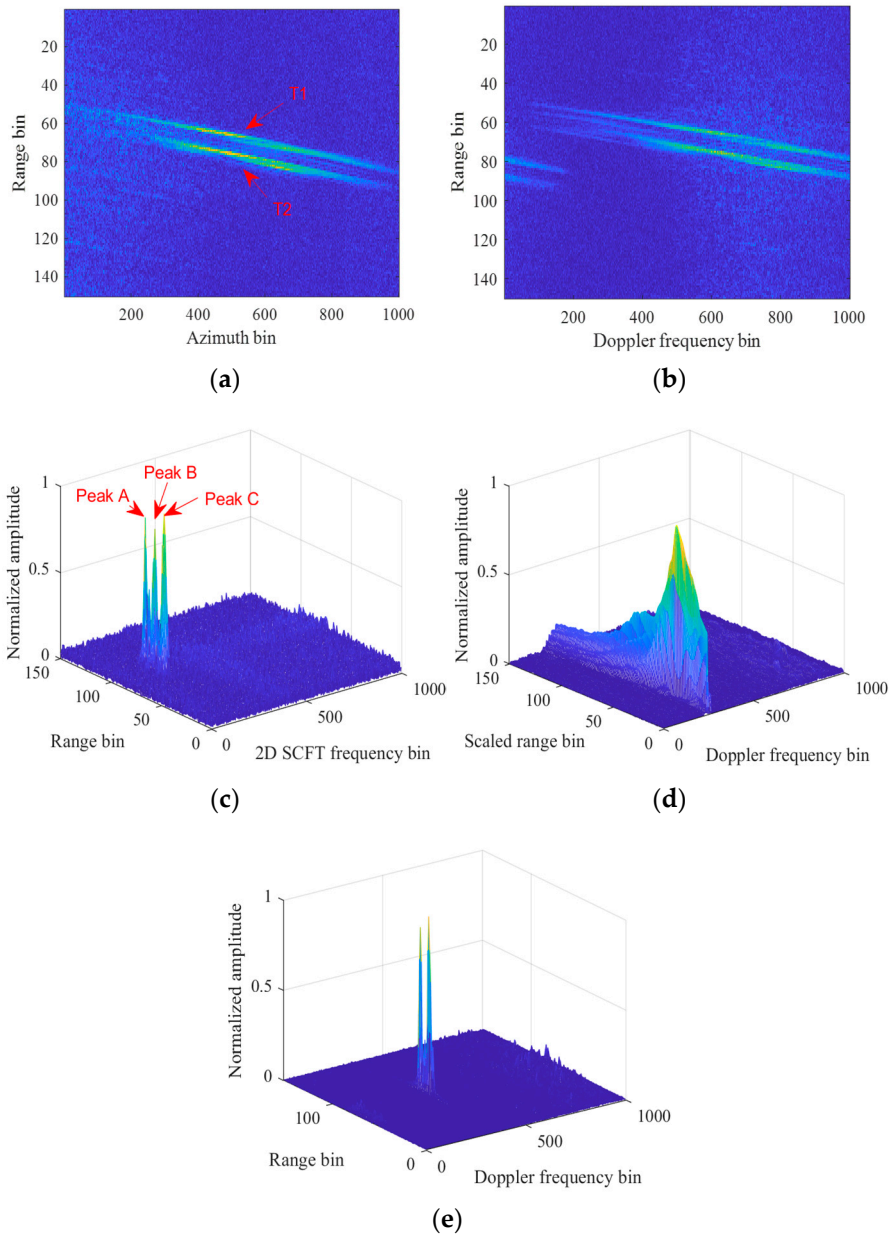

Figure 8. Spaceborne real data results of two targets. (**a**) Scene of the selected data for two targets. (**b**) Result of range compression. (**c**) Result of SCFT. (**d**) Result of SCIFT. (**e**) Focusing result of the target by the developed approach.

3.3. Airborne Real Data Result

The validity of this method is verified by X-band, three-channel real airborne SAR data. The parameters of X-band SAR are listed in Table 5.

Table 5. Basis radar parameters of airborne real data.

Parameters	Value
Carrier frequency	8.85 GHz
Range bandwidth	40 MHz
Pulse repetition frequency	1000 Hz

The image of the selected airborne data in the range-Doppler domain is shown in Figure 9a. It can be seen that there is strong ground clutter in the scene. Then, the extended

factor method in [35] is used for suppressing the ground clutter, and the result is shown in Figure 9b. Figure 9b shows that the target is severely defocused in the range-Doppler domain. Figure 9c shows the result after SCFT processing, and the second-order phase coefficient can be obtained from the peak position. After SCIFT and phase compensation function processing, as shown in Figure 9d, the first-order phase coefficient can be estimated. With the estimated first- and second-order phase coefficient, the matched filtering function shown in (13) is constructed. Figure 9e shows the result of processing the target signal using the constructed matched filter function, and the target is effectively focused. According to the experiments, the Doppler parameters of the selected moving target are as follows: $\rho_0 = -2.5$, $\rho_1 = 0.7598$. Figure 9g shows the processing result of the selected moving target using the DKP method [20]. As can be seen from Figure 9g, the target energy shows an obvious defocusing phenomenon, and the focusing performance is significantly reduced, because the DKP method ignores the influence of the along-track velocity of the moving target. The above results can confirm that the presented method is superior to the DKP method.

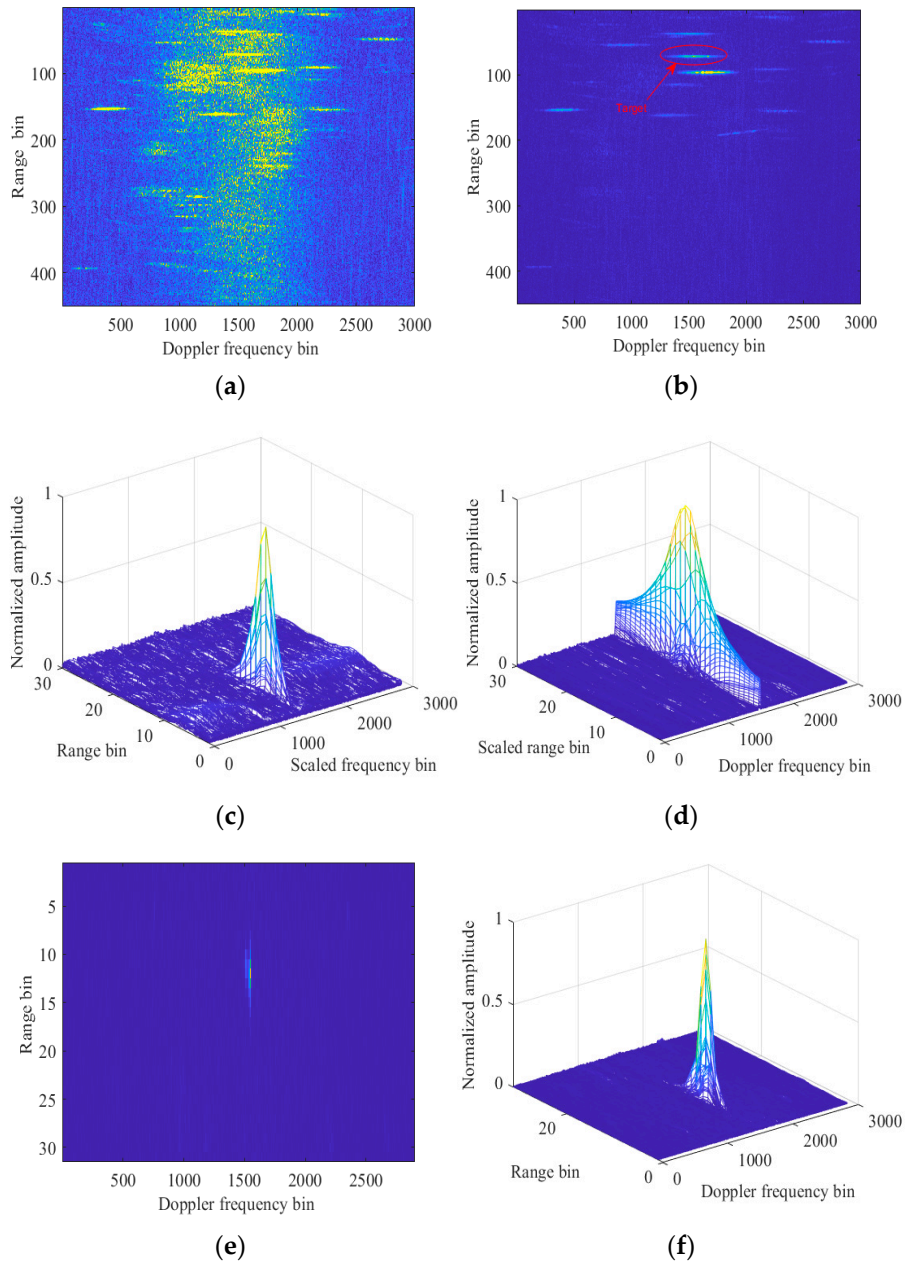

Figure 9. *Cont.*

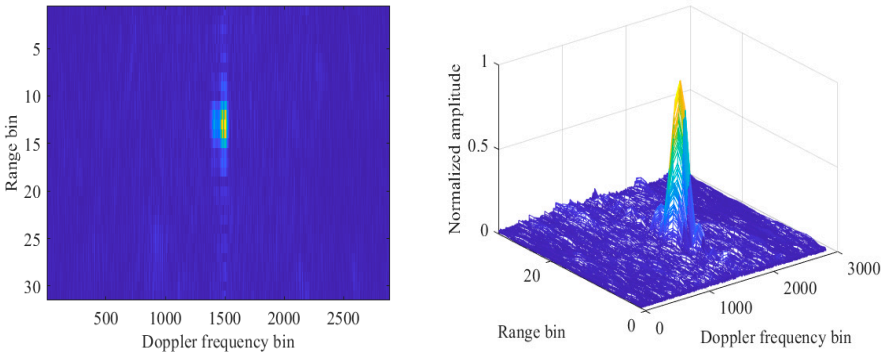

(**g**) (**h**)

Figure 9. Results of airborne measured data. (**a**) Airborne SAR data scene without clutter suppression. (**b**) Result after clutter suppression. (**c**) Results of SCFT. (**d**) Results of SCIFT. (**e**) The result of focusing the target with the developed approach. (**f**) Stereogram of Figure 9e. (**g**) The result of focusing the target using the DKP method [20]. (**h**) Stereogram of Figure 9g.

4. Discussion

In this section, the computational complexity of the proposed algorithm is analyzed and compared with the IAR-TRT [14], the KT-based method [30], the 2-DFMF-based method [21], the MSOKT [17], and the DKP [20]. We assume that N, M are the numbers of the azimuth pulses and range units, respectively. N_a, N_b, and N_c are, respectively, the searching numbers of the Doppler ambiguity number, the MSOKT, and the IAR-TRT methods. The proposed method mainly includes three steps. Firstly, the SCFT is used to realize the second-order phase coefficient estimation. The computational complexity of the SCFT operation implemented by a nonuniform fast Fourier transform is $O(MN\log_2 N)$ [36–38]; therefore, the computational cost of this step is $O(MN\log_2 N + NM\log_2 M)$. The second step is the first-order phase coefficient estimation, and the computational cost of the SCIFT operation is implemented by a chirp-z transform is $O(3NM\log_2 M)$ [39]. Then, the computational cost of the second step is $O(3NM\log_2 M + MN\log_2 N)$. The third step is range time domain azimuth-frequency domain focusing, and the computational cost of this step is $O(MN\log_2 N + NM\log_2 M)$. In summary, the computational complexity of the proposed method is expressed as $O(3MN\log_2 N + 5NM\log_2 M)$. According to the method description detailed in [14], the main computational complexity of the IAR-TRT method is denoted as $O((N_c+4)MN\log_2 N)$. Furthermore, for the DKP method detailed in [20], its computational complexity is expressed as $O(MN^2 + N(N-1)M + (N_a+1)(MN\log_2 N + MN\log_2 M)$. The main computational complexity of the 2-DFMF-based method [21] can be expressed as $O((N_a+2)(MN\log_2 N + MN\log_2 M) + MN)$. For the MSOKT method proposed in [17], its computational complexity can be expressed as $O((N_b+1)MN\log_2 N)$. For the KT-based method proposed in [30], the main computational complexity is expressed as $O(MN^2 + MN(N-1) + N_a(MN + MN\log_2 N + MN\log_2 M))$. The computational complexity of the above six methods is shown in Table 6. Figure 10 shows the relationship curve of the computational complexity of the six methods with the number of azimuth pulses. In general, the computational complexity of the proposed algorithm is the lowest among the six methods.

Table 6. Computational complexities of the six methods.

Methods	Computational Complexity
Proposed method	$O(5MN\log_2 M + 3MN\log_2 N)$
MSOKT-based method	$O((N_b+1)MN\log_2 N)$
DKP-based method	$O(MN^2 + N(N-1)M + (N_a+1)(MN\log_2 N + MN\log_2 M)$
IAR-TRT method	$O((N_c+4)MN\log_2 N)$
KT-based method	$O(MN^2 + MN(N-1) + N_a(MN + MN\log_2 N + MN\log_2 M))$
2-DFMF-based method	$O((N_a+2)(MN\log_2 N + MN\log_2 M) + MN)$

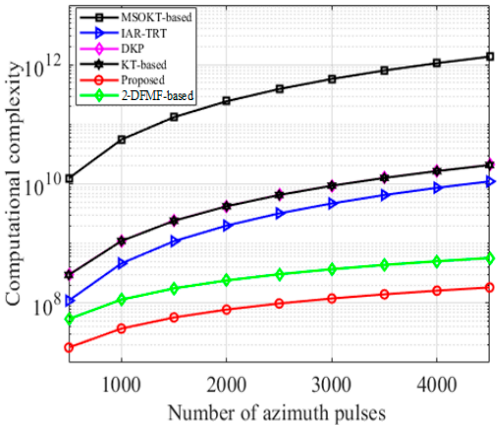

Figure 10. A computational complexity diagram of the six methods.

5. Conclusions

Severe DFS and RCM caused by unknown relative motion of radar and moving targets are the main reasons for the defocusing effect of a target. In addition, due to the limitation of the repetition frequency of SAR, for the moving target signal, it is easy to show Doppler ambiguity. Doppler ambiguity will make RCM and DFS compensation more difficult. Therefore, in the case of Doppler ambiguity, the RCM and DFS can also be effectively compensated, so that the target can be accurately focused. To solve these problems, this article proposes a computational efficient SAR ground moving target imaging method based on SCFT and SCIFT. The main properties of the proposed algorithm can be summarized as follows: (1) the presented method can effectively correct RCM and DFS and obtain a well-focused result; (2) the proposed method has strong Doppler ambiguity tolerance (including Doppler spectrum splitting and Doppler center ambiguity); (3) the proposed method has a low computational cost because the searching steps for ambiguity numbers and unknown target parameters can be avoided; (4) the problem of BSSL is effectively handled; and (5) the identification procedure of a spurious peak is given for the cross term problem in case of multiple targets, according to the analysis of the features of the cross terms in detail. Finally, the experimental results of real spaceborne and airborne data are given in order to verify the effectiveness of the proposed method.

However, the proposed method is suitable for the imaging of uniform moving targets with a second-order range model. In addition, the proposed moving target imaging method and the operation of the spurious peak recognition both include the nonlinear transform. The performance of moving target imaging and spurious peak recognition will degrade under the low SNR situation. Therefore, the computationally efficient method for imaging of non-uniform moving targets with a high order (more than second-order) range model under the low SNR circumstance will become a research direction in the future.

Author Contributions: Conceptualization, X.Z., J.W. and H.Z.; data curation, J.W., X.Z. and R.L.; software, H.Z.; formal analysis, X.Z. and J.W.; funding acquisition, J.W. and Z.C.; investigation, H.Z. and R.L.; methodology, J.W., X.Z. and H.Z.; project administration, Z.C.; supervision, J.W.; validation, J.W., X.Z. and R.L.; writing—original draft, X.Z. and H.Z.; writing—review and editing, J.W., R.L. and Z.C. All authors have read and agreed to the published version of the manuscript.

Funding: This research was funded by the National Natural Science Foundation of China, under Grant 62201099, Grant 62001062, and Grant U20A20157; the Key Research and Development Program of Jiangsu Province, under Grant BE2023021; the Opening Project of Guangxi Key Laboratory of Wireless Wideband Communication and Signal Processing under Grant GXKL06230203.

Data Availability Statement: The data that support the findings of this study are available from the corresponding author upon reasonable request.

Conflicts of Interest: The authors declare no conflicts of interest.

Appendix A

In this section, the selection criteria of zoom factor φ will be elaborated on in detail. We assume that the value scope of the target along-track velocity is $[-v_{a\max}, v_{a\max}]$, and can obtain the following:

$$\rho_1 = \frac{(v - v_a)^2}{2R_0} \leq \frac{(v + v_{a\max})^2}{2R_0} \tag{A1}$$

According to the peak value in (7), we can obtain the following:

$$f_\psi = -\frac{4\rho_1}{\varphi\lambda} \tag{A2}$$

In order for the zoom factor φ to match, the following inequality should be satisfied:

$$f_{\psi\max} \geq \left|\frac{4\rho_1}{\varphi\lambda}\right|_{\max} = \frac{2(v + v_{a\max})^2}{\varphi\lambda R_0} \tag{A3}$$

where $f_{\psi\max}$ represents the maximum value of f_ψ.

Therefore, we can obtain the following:

$$\varphi \geq \frac{2(v + v_{a\max})^2}{\lambda R_0 f_{\psi\max}} \tag{A4}$$

According to the above analysis, as long as the zoom factor selected is as small as possible under the condition of satisfying (A4), the error can be reduced, and the accuracy of parameter estimation can be improved.

References

1. Cumming, I.G.; Wong, F.H. *Digital Processing of Synthetic Aperture Radar Data: Algorithm and Implementation*; Artech House: Norwood, MA, USA, 2005.
2. Moreira, A.; Iraola, P.P.; Younis, M.; Krieger, G.; Hajnsek, I.; Papathanassiou, K.P. A tutorial on synthetic aperture radar. *IEEE Geosci. Remote Sens. Mag.* **2013**, *1*, 6–43. [CrossRef]
3. Chen, Z.; Tang, S.; Ren, Y.; Guo, P.; Zhou, Y.; Huang, Y.; Wan, J.; Zhang, L. Curvilinear Flight Synthetic Aperture Radar (CF-SAR): Principles, Methods, Applications, Challenges and Trends. *Remote Sens.* **2022**, *14*, 2983. [CrossRef]
4. Guo, Y.; Li, Q.; Zhang, L.; Zhang, J.; Chen, Z. An Oblique Projection-Based Beamforming Method for Coherent Signals Receiving. *Remote Sens.* **2022**, *14*, 5043. [CrossRef]
5. Kim, D.; Lee, H.; Jung, H.C.; Hwang, E.; Hossain, F.; Bonnema, M.; Kang, D.H.; Getirana, A. Monitoring River Basin Development and Variation in Water Resources in Transboundary Imjin River in North and South Korea Using Remote Sensing. *Remote Sens.* **2020**, *12*, 195. [CrossRef]
6. Shi, W.; Zhang, M.; Zhang, R.; Chen, S.; Zhan, Z. Change detection based on artificial intelligence: State-of-the-art and challenges. *Remote Sens.* **2020**, *12*, 1688. [CrossRef]
7. Liu, N.; Ge, G.; Tang, S.; Zhang, L. Signal Modeling and Analysis for Elevation Frequency Scanning HRWS SAR. *IEEE Trans. Geosci. Remote Sens.* **2020**, *58*, 6434–6450.
8. Tang, S.; Guo, P.; Zhang, L.; So, H.C. Focusing hypersonic vehicle-borne SAR data using radius/angle algorithm. *IEEE Trans. Geosci. Remote Sens.* **2020**, *58*, 281–293. [CrossRef]
9. You, D.; Sun, G.; Xia, X.; Xing, M.; Li, B.; Bao, Z. Time-varying baseline error estimation and compensation in UAV SAR interferometry based on time-domain subap-erture of raw radar data. *IEEE Sensors J.* **2020**, *20*, 12203–12216. [CrossRef]
10. Alver, M.B.; Saleem, A.; Cetin, M. Plug-and-play synthetic aperture radar image formation using deep priors. *IEEE Trans. Comput. Imaging* **2021**, *7*, 43–57. [CrossRef]
11. Huang, Y.; Liao, G.; Xu, J.; Li, J.; Yang, D. GMTI and parameter estimation for MIMO SAR system via fast interferometry RPCA method. *IEEE Trans. Geosci. Remote Sens.* **2018**, *56*, 1774–1787. [CrossRef]
12. Wan, J.; Chen, Z.; Zhou, Y.; Li, D.; Huang, Y.; Zhang, L. Ground moving target imaging based on MSOKT and KT for synthetic aperture radar. In Proceedings of the IEEE International Geoscience Remote Sensing Symposium, Waikoloa, HI, USA, 26 September–2 October 2020; pp. 2141–2144.
13. Chen, Z.; Zhou, Y.; Zhang, L.; Wei, H.; Lin, C.; Liu, N.; Wan, J. General range model for multi-channel SAR/GMTI with curvilinear flight trajectory. *Electron. Lett.* **2019**, *55*, 111–112. [CrossRef]

14. Huang, P.; Xia, X.G.; Liu, X.; Liao, G. Refocusing and motion parameter estimation for ground moving targets based on improved axis rotation-time reversal transform. *IEEE Trans. Comput. Imaging* **2018**, *4*, 479–494. [CrossRef]
15. Chen, Z.; Zhou, S.; Wang, X.; Huang, Y.; Wan, J.; Li, D.; Tan, X. Single range data-based clutter suppression method for multichannel SAR. *IEEE Geosci. Remote Sens. Lett.* **2022**, *19*, 1–5.
16. Chang, X.; Li, Y.; Zhao, Y. An improved scattered wave deceptive jamming method based on a moving jammer beam footprint against a three-channel short-time SAR GMTI. *IEEE Sens. J.* **2021**, *21*, 4488–4499. [CrossRef]
17. Wan, J.; Zhou, Y.; Zhang, L.; Chen, Z. Ground moving target focusing and motion parameter estimation method via MSOKT for synthetic aperture radar. *IET Signal Process.* **2019**, *13*, 528–537. [CrossRef]
18. Dong, Q.; Xing, M.; Xia, X.; Zhang, S.; Sun, G. Moving target refocusing algorithm in 2-D wavenumber domain after BP integral. *IEEE Geosci. Remote Sens. Lett.* **2018**, *15*, 127–131. [CrossRef]
19. Lin, L.; Sun, G.; Cheng, Z.; He, Z. Long-time coherent integration for maneuvering target detection based on ITRT-MRFT. *IEEE Sens. J.* **2020**, *20*, 3718–3731. [CrossRef]
20. Sun, G.; Xing, M.; Xia, X.G.; Wu, Y.; Bao, Z. Robust ground moving-target imaging using deramp-Keystone processing. *IEEE Trans. Geosci. Remote Sens.* **2013**, *51*, 966–982. [CrossRef]
21. Zhu, S.; Liao, G.; Qu, Y.; Zhou, Z.; Liu, X. Ground moving targets imaging algorithm for synthetic aperture radar. *IEEE Trans. Geosci. Remote Sens.* **2011**, *49*, 462–477. [CrossRef]
22. Wan, J.; Tan, X.; Chen, Z.; Li, D.; Liu, Q.; Zhou, Y.; Zhang, L. Refocusing of ground moving targets with Doppler ambiguity using Keystone transform and modified second-order Keystone transform for synthetic aperture radar. *Remote Sens.* **2021**, *13*, 177. [CrossRef]
23. Perry, R.P.; DiPietro, R.C.; Fante, R.L. SAR imaging of moving targets. *IEEE Trans. Aerosp. Electron. Syst.* **1999**, *35*, 188–200. [CrossRef]
24. Zhu, D.; Li, Y.; Zhu, Z. A keystone transform without interpolation for SAR ground moving-target imaging. *IEEE Geosci. Remote Sens. Lett.* **2007**, *4*, 18–22. [CrossRef]
25. Dai, Z.; Zhang, X.; Fang, H.; Bai, Y. High accuracy velocity measurement based on keystone transform using entropy minimization. *Chin. J. Electron.* **2016**, *25*, 774–778. [CrossRef]
26. Kirkland, D. Imaging moving targets using the second-order keystone transform. *IET Radar Sonar Navig.* **2011**, *5*, 902–910. [CrossRef]
27. Zhou, F.; Wu, R.; Xing, M. Approach for single channel SAR ground moving target imaging and motion parameter estimation. *IET Radar Sonar Navig.* **2007**, *1*, 59–66. [CrossRef]
28. Li, G.; Xia, X.G.; Peng, Y. Doppler keystone transform: An approach suitable for parallel implementation of SAR moving target imaging. *IEEE Geosci. Remote Sens. Lett.* **2008**, *5*, 573–577. [CrossRef]
29. Huang, P.; Liao, G.; Yang, Z.; Xia, X.; Ma, J.; Ma, J. Long-time coherent integration for weak maneuvering target detection and high-order motion parameter estimation based on keystone transform. *IEEE Trans. Signal Process.* **2016**, *64*, 4013–4026. [CrossRef]
30. Huang, P.; Liao, G.; Yang, Z.; Xia, X.G.; Ma, J.; Zhang, X. An approach for refocusing of ground moving target without motion parameter estimation. *IEEE Trans. Geosci. Remote Sens.* **2017**, *55*, 336–350. [CrossRef]
31. Tian, J.; Cui, W.; Xia, X.G.; Wu, S. Parameter estimation of ground moving targets based on SKT-DLVT processing. *IEEE Trans. Comput. Imaging* **2016**, *2*, 13–26. [CrossRef]
32. Chen, X.; Guan, J.; Liu, N.; He, Y. Maneuvering target detection via Radon-fractional Fourier transform-based long-time coherent integration. *IEEE Trans. Signal Process.* **2014**, *62*, 939–953. [CrossRef]
33. Chen, X.; Guan, J.; Liu, N.; Zhou, W.; He, Y. Detection of a low observable sea-surface target with micromotion via Radon-linear canonical transform. *IEEE Geosci. Remote Sens. Lett.* **2014**, *11*, 1125–1129.
34. Li, X.; Sun, Z.; Yeo, T.S. Computational efficient refocusing and estimation method for radar moving target with unknown time information. *IEEE Trans. Comput. Imaging* **2020**, *6*, 544–557. [CrossRef]
35. DiPietro, R.C. Extended factored space-time processing for airborne radar systems. In Proceedings of the Twenty-Sixth Asilomar Conference on Signals, Systems & Computers, Pacific Grove, CA, USA, 26–28 October 1992; pp. 425–430.
36. Liu, Q.H.; Nguyen, N. An accurate algorithm for nonuniform fast Fourier transforms (NUFFT's). *IEEE Microw. Guid. Wave Lett.* **1998**, *8*, 18–20. [CrossRef]
37. Liu, Q.H.; Nguyen, N.; Tang, X.Y. Accurate algorithms for nonuniform fast forward and inverse Fourier transforms and their applications. In Proceedings of the IEEE International Geoscience Remote Sensing Symposium, Seattle, DC, USA, 6–10 July 1998; pp. 288–290.
38. Song, J.Y.; Liu, Q.H.; Torrione, P.; Collins, L. Two-dimensional and three-dimensional NUFFT migration method for landmine detection using ground-penetrating radar. *IEEE Trans. Geosci. Remote Sens.* **2006**, *44*, 1462–1469. [CrossRef]
39. Zheng, J.; Su, T.; Zhu, W.; He, X.; Liu, Q. Radar High-Speed Target Detection Based on the Scaled Inverse Fourier Transform. *IEEE J. Sel. Top. Appl. Earth Observ. Remote Sens.* **2015**, *8*, 1108–1119. [CrossRef]